324-MHz interdigital H-mode drift tube linac for muon acceleration

Y. Nakazawa,[1,*] Y. Ibaraki,[2,†] E. Cicek,[1] K. Futatsukawa,[1] Y. Fuwa,[3] N. Hayashizaki,[4] T. Iijima,[2,5] H. Iinuma,[6] Y. Iwata,[7] Y. Kondo,[3,6] T. Mibe,[1] S. Mizobata,[1] T. Morishita,[3] M. Otani,[1] K. Sumi,[1] and Y. Takeuchi[2]

[1]*High Energy Accelerator Research Organization (KEK), Tsukuba, Ibaraki, 305-0801, Japan*
[2]*Graduate School of Science, Nagoya University, Nagoya, Aichi 464-8602, Japan*
[3]*Japan Atomic Energy Agency (JAEA), Tokai, Naka, Ibaraki, 319-1195, Japan*
[4]*Tokyo Institute of Technology, Tokyo, 152-8550, Japan*
[5]*Kobayashi-Maskawa Institute (KMI), Nagoya University, Nagoya, Aichi 464-8602, Japan*
[6]*Graduate School of Science and Engineering, Ibaraki University, Mito, Ibaraki, 310-8512, Japan*
[7]*National Institutes for Quantum Science and Technology, 4-9-1 Anagawa, Inage, Chiba 263-8555, Japan*

(Received 22 June 2026; accepted 4 August 2026; published 1 September 2026)

We have constructed a 324-MHz interdigital H-mode drift tube linear accelerator (IH-DTL) with an alternating phase focusing method. This IH-DTL will be part of a muon linear accelerator (linac) being developed at the Japan Proton Accelerator Research Complex for a precise measurement of the muon anomalous magnetic moment and a search for the muon electric dipole moment. The IH-DTL is 1.45 m long and accelerates muons from $\beta = v/c = 0.08$ to 0.28. Low-power tuning was performed using six slug tuners, which reduced the peak-to-peak on-axis field error to 1.4%. Following 94 h of high-power conditioning, the IH-DTL demonstrated stable operation at the nominal peak power of 390 kW and a duty factor of 0.1%, corresponding to the designed accelerating field (E_0) of 3.6 MV/m. This paper presents the construction, low-power rf tuning, and high-power performance of the 324-MHz IH-DTL.

DOI: 10.1103/1l3t-rvmf

I. INTRODUCTION

The muon anomalous magnetic moment $(g-2)$ is a sensitive probe for possible physics beyond the Standard Model (SM). Recent experimental measurements with sub-ppm precision [1] have attracted considerable attention because of a possible discrepancy between experiment and the SM prediction [2]. At the same time, theoretical studies of the muon $g-2$ are actively progressing [3]. Although the comparison between experiment and theory remains under discussion, further measurements based on independent experimental principles and different systematic uncertainties are strongly motivated. A new muon $g-2$ experiment at the Japan Proton Accelerator Research Complex (J-PARC), referred to as the E34 experiment [4], is being planned. The E34 experiment employs a low-emittance muon beam, which enables the use of a compact storage magnet without electric-field focusing. This approach provides such an independent measurement with systematic uncertainties different from those of previous muon $g-2$ experiments. The experiment aims at sub-ppm precision in the muon $g-2$ measurement and a sensitivity on the order of 10^{-21} $e \times \mathrm{cm}$ in the search for the muon electric dipole moment (EDM).

The E34 experiment requires low-emittance muon beams accelerated to an energy of 212 MeV, corresponding to a velocity $\beta (= v/c)$ of 0.95, for efficient injection into the compact 3 T storage magnet. The required total transverse emittance is approximately 1.5π mm mrad [5]. To fulfill these requirements, we use ultraslow muons with an energy of 30 meV produced by the laser ionization of thermal muonium in a vacuum [6–8]. Four types of radio-frequency (rf) linear accelerators (linacs) accelerate the ultraslow muons up to an energy of 212 MeV [4,5]. Rapid acceleration using linacs is essential because muons have a finite lifetime of 2.2 μs. Beyond the E34 experiment, low-emittance muon beams produced by linacs are also an essential technology for a transmission muon microscope [9]. Initial studies of rf bunching and acceleration using a radio-frequency quadrupole (RFQ) linac were carried out in 2017–2019 with negative muonium ions [10,11]. More recently, the first rf acceleration of positive muons was successfully demonstrated using the RFQ linac [12].

In the low β region following RFQ, an rf cavity with a high effective acceleration gradient is preferable to minimize muon decay losses. Several cavity options, including

*Contact author: yuga.nakazawa@kek.jp
†Contact author: yuka.ibaraki122602@gmail.com

TABLE I. Main parameters of the 324-MHz APF IH-DTL.

Parameters	Values
Beam species	μ^+
Beam intensity	$1 \times 10^6/\mathrm{s}$
Beam pulse width	10 ns
Resonant frequency	324 MHz
Repetition rate	25 Hz
rf pulse width	40 μs
Duty factor	0.1%
Synchronous phase	$-44°$ to $+48°$
Number of cells	16
Total length	1.45 m
Injection energy	0.34 MeV
Extraction energy	4.26 MeV

the Alvarez DTL, CH-DTL, and IH-DTL, were compared for this velocity range [13]. Based on this comparison, we employed a 324-MHz interdigital H-mode drift tube linac (IH-DTL) because of its cost-effective cavity structure. The IH-DTL was designed to accelerate muons from $\beta = 0.08$ to 0.28 [14]. An alternating phase focusing (APF) method [15] was adopted to reduce construction costs. It is one of the transverse focusing methods, and an rf transverse force is obtained by alternating positive and negative synchronous phases. As a result, no focusing elements need to be installed inside the cavity. The alternating synchronous phases reduce acceleration efficiency, but the H-mode structure, which allows high effective shunt impedance, compensates for it. Although the APF method is generally applicable only to low-current beams [16–18], the muon beam intensity in the muon linac is very low ($\sim 10^6\ \mu^+/s$), so the focusing provided by the APF method is sufficient.

The 324-MHz APF IH-DTL employs a three-piece configuration comprising a center plate and two semi-cylindrical side shells constructed from oxygen-free copper [19]. All drift tubes are monolithically machined on the center plate; no surface treatment is required. The feasibility of this cost-effective fabrication method and stable high-power operation were previously demonstrated using a short-length prototype cavity [20]. Based on the dynamics design in Ref. [14] and the experience with the prototype development described above, the first full-size 324-MHz APF IH-DTL for the E34 experiment was developed. Nevertheless, the first full-size cavity requires careful field tuning because of the relatively small muon mass. In particular, the peak-to-peak on-axis field error for each cell must be reduced to less than 4%, as required by the beam dynamics design [14]. At the same time, it is critical to tune the resonant frequency to 324.00 ± 0.01 MHz, since small frequency deviations can be compensated by cooling-water temperature control [21].

This paper describes the development and performance evaluation of the first full-size 324-MHz APF IH-DTL dedicated to muon acceleration. Section II presents the detailed structure of the IH-DTL based on the dynamics design in Ref. [14]. Section III describes the results of the low-power measurements and rf tuning using slug tuners. The high-power test of the IH-DTL with a water-cooling system is described in Sec. IV. The paper concludes with a summary of the findings in Sec. V.

II. DESIGN OF THE IH-DTL

The beam-dynamics design of the APF IH-DTL was based on Ref. [14]. The IH-DTL has 16 cells, and the synchronous phases for each cell range from $-44°$ to $+48°$. The cells with a negative synchronous phase focus the beam longitudinally, while those with a positive synchronous phase focus the beam transversely. The IH-DTL has a total length of 1.45 m and no internal focusing elements. This IH-DTL accelerates muons from an energy of 0.34 to 4.26 MeV. The main parameters are presented in Table I.

The rf design of the IH-DTL was performed using `CST MICROWAVE STUDIO (MWS)` [22]. Figure 1 shows the side view of the cavity. The cavity has a cylindrical structure that can be easily fabricated in a three-piece design [19]. The cavity length (L_c), drift tube length (L_DT),

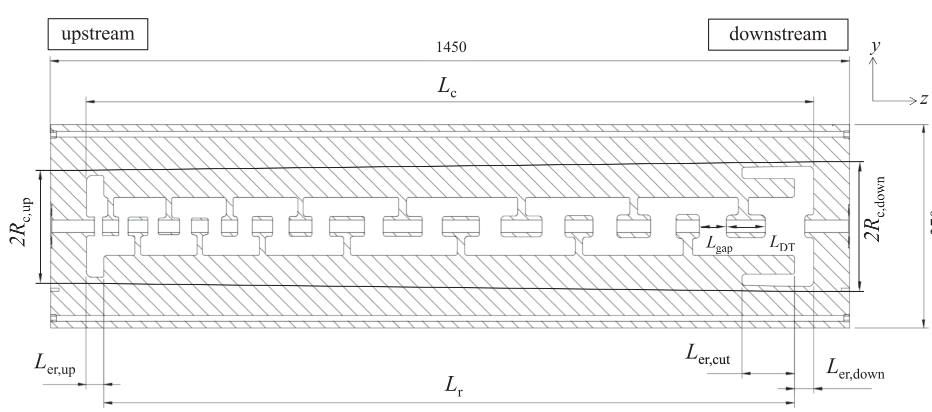

FIG. 1. Side view of the center plate.

TABLE II. Dimensions of the cavity structure in the IH-DTL [21].

Parameters		Values (mm)
L_c	Cavity length	1320.0
$R_{c,up}$	Upstream cavity radius	102.6
$R_{c,down}$	Downstream cavity radius	118.2
L_r	Ridge length	1253.2
$L_{er,up}$	End ridge length	31.8
$L_{er,down}$	End ridge length	35.0
$L_{er,cut}$	End ridge cut length	94.9

and gap length (L_{gap}) were determined by taking into account dynamics calculations [14]. The upstream and downstream cavity radii ($R_{c,up}$, $R_{c,down}$), the ridge length (L_r), the upstream and downstream end-ridge lengths ($L_{er,up}$, $L_{er,down}$), and the end-ridge cut length ($L_{er,cut}$) were modified from Ref. [14]. These modifications were made to achieve a flat electric field distribution and tune the frequency. Table II shows the dimensions of the cavity structure.

Figure 2 shows an enlarged view of the drift tube and stem of the IH-DTL. The inner radius of the drift tube ($R_{DT,in}$) was determined from the transverse beam size obtained based on the numerical calculations [14]. Note that $R_{DT,in}$ and the inner edge radius of the drift tube ($r_{edge,in}$) must be uniform for all drift tubes due to machining constraints. Fine-tuning of the field strength at each gap was conducted by adjusting the radius of the stem (R_{stem}) and the outer radius of the drift tube ($R_{DT,out}$). The outer edge radius of the drift tube ($r_{edge,out}$) was determined to reduce the surface rf field. The dimensions of the drift tube were also modified from Ref. [14] for the above reasons. The dimensions of the drift tubes for each cell are summarized in Table III.

The resonant frequency of the bare cavity was set to 322.38 MHz, marginally below the operating frequency to

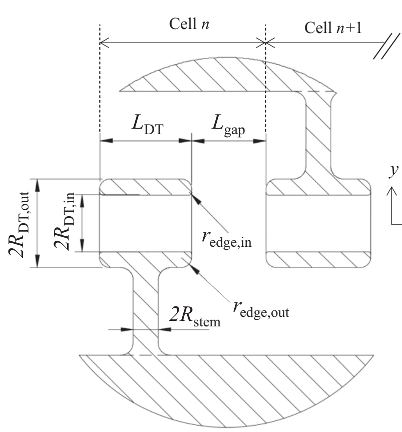

FIG. 2. Enlarged view of the drift tube and stem on the center plate.

TABLE III. Dimensions of the IH-DTL cells [21].

Cell no.	R_{stem} (mm)	$R_{DT,in}$ (mm)	$R_{DT,out}$ (mm)	$r_{edge,in}$ (mm)	$r_{edge,out}$ (mm)
0		11.4	17.20	1.0	2.2
1	5.00	11.4	17.30	1.0	2.7
2	5.00	11.4	17.20	1.0	2.9
3	5.00	11.4	15.30	1.0	2.8
4	5.00	11.4	15.40	1.0	2.8
5	6.00	11.4	17.60	1.0	3.8
6	5.00	11.4	17.80	1.0	4.0
7	5.00	11.4	17.80	1.0	4.0
8	6.00	11.4	18.00	1.0	4.0
9	7.00	11.4	18.10	1.0	4.6
10	7.00	11.4	18.05	1.0	5.2
11	7.00	11.4	19.00	1.0	5.7
12	7.00	11.4	19.60	1.0	5.8
13	6.75	11.4	20.50	1.0	6.0
14	8.50	11.4	21.50	1.0	7.0
15	9.00	11.4	21.00	1.0	7.6
16		11.4	21.00	1.0	7.7

allow for tuning. The unloaded quality factor (Q_0) was simulated to be 10910. The nominal peak power calculated from the simulated Q_0 was 310 kW, and the effective shunt impedance was 65 MΩ/m. The maximum surface field was 35.4 MV/m, corresponding to 2.0 times the Kilpatrick limit [23]. This value was obtained at the surface of the 13th drift tube. The mesh convergence was confirmed by varying the tetrahedral mesh fineness and checking the stability of the resonant frequency and Q_0. The eigenmode calculation in CST MWS used approximately 3×10^6 tetrahedral mesh cells.

Figure 3 shows the simulated on-axis electromagnetic field distribution of the IH-DTL using CST MWS. Here, the

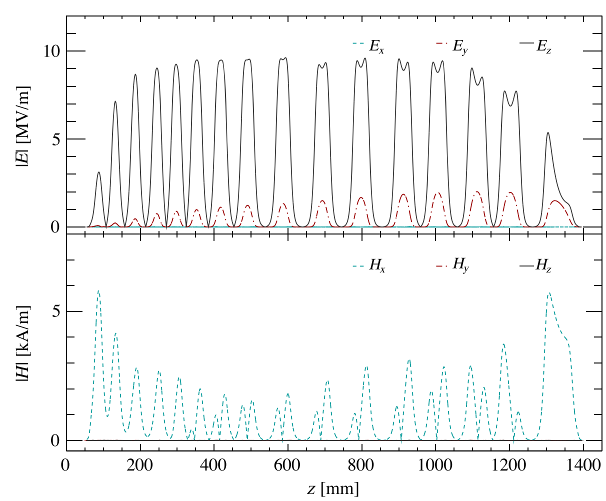

FIG. 3. Simulated on-axis electromagnetic field distribution of the IH-DTL. The accelerating field is 3.6 MV/m on average. This figure is reproduced from Ref. [21].

x direction is horizontal, and the y direction is vertical with respect to the cavity orientation shown in Fig. 1. The nominal accelerating field gradient (E_0) is 3.6 MV/m on average. The IH-DTL has not only an accelerating field (E_z) but also nonzero transverse field components (H_x and E_y) due to the characteristics of the H-mode cavity. The ratio of the magnitude of E_y to E_z for each gap is in the range of 2% to 28%. Several solutions were considered to reduce this E_y, including the use of drift tube bulges [14]. However, this method reduces the transverse field by only a few percent. Because the additional device would induce extra power loss, we decided to mount no additional structure in this design.

After designing the rf structure, the electromagnetic field simulated by CST MWS was implemented in `General Particle Tracer` (GPT) [24] to calculate the beam dynamics numerically. Figure 4 shows the phase-space distribution at the IH-DTL exit. The input particle distribution for this simulation was obtained from the simulated distribution at the medium-energy beam transport line (MEBT) exit downstream of the RFQ [25]. The normalized root mean square (rms) emittance at the IH-DTL exit was calculated to be $0.26\,\pi$ and $0.25\,\pi$ mm mrad in the x and y directions, respectively. The emittance growths in the x and y direction from the MEBT exit were 8.4% and 5.9%, respectively. The total beam transmission rate, including the muon decay loss, was 98.9%. These results satisfy the beam-dynamics requirements for the IH-DTL in the muon linac. The calculated rf characteristics and the beam parameters at the IH-DTL exit are summarized in Table IV.

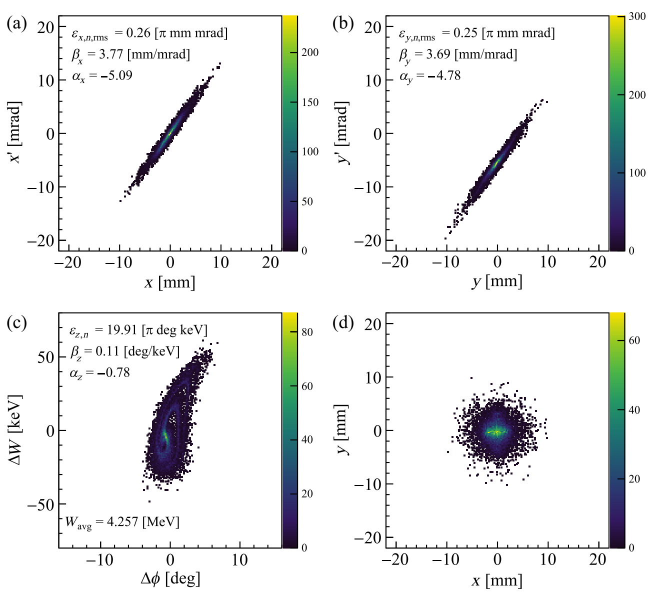

FIG. 4. Simulated phase-space distributions at the IH-DTL exit. (a) Divergence angle x' vs position x, (b) y' vs y, (c) Energy spread $\Delta W\ (= W - 4.26$ MeV) vs phase spread $\Delta\phi$, (d) y vs x.

TABLE IV. Calculated parameters of the IH-DTL.

Parameters	Values
Unloaded quality factor (Q_0)	10910
Resonant frequency (bare cavity)	322.38 MHz
Accelerating field on average	3.6 MV/m
Maximum surface field	35.4 MV/m (2.0 E_k[a])
Nominal peak power	310 kW[b]
Shunt impedance	65 MΩ/m
Extraction energy	4.26 MeV
Horizontal emittance growth	8.4%
Vertical emittance growth	5.9%
Transmission rate	100%
Transient time	25 ns
Decay loss	1.1%
Total transmission rate	98.9%

[a]Kilpatrick limit.
[b]Calculated from a simulated Q_0.

Figure 5 shows the cross-sectional front view of the mechanical structure of the IH-DTL. The cavity consists of three pieces. Each piece is made of oxygen-free copper in class 1. Two side shells and a center plate with a 90 mm width were bolted together. Drift tubes were machined monolithically on the center plate. A beryllium-copper coil spring was used for rf contact, and a Viton O-ring was used to seal the vacuum. Two water-cooling channels with a diameter of ϕ10 mm were integrated into each of the three cavity pieces, resulting in six straight channels from the upstream to the downstream end of the cavity. The designed peak power dissipation of the IH-DTL is 310 kW, while the duty factor is as low as 0.1%. Therefore, direct cooling of the drift tubes and stems was not adopted; instead, these channels provide indirect cooling of the monolithic drift tubes through the center plate.

The top view of the mechanical structure is shown in Fig. 6. The side shells have six slug tuner ports, one rf coupler port, three pickup ports, and two vacuum pumping ports with a slit. The diameter of the tuner is ϕ58 mm. The tuner stroke length is 50 mm with a positioning accuracy of 0.01 mm. The tuner insertion length is defined from the outer surface of the side shell; therefore, $L_\mathrm{t} = 0$ corresponds to the position before insertion into the tuner port. Because the inner surface of the side shell is inclined, the insertion length corresponding to the flush position varies among the tuner locations and is approximately $L_\mathrm{t} = 30$ mm. The number of tuner ports was set to six because of size limitations on tuners and other devices. The tuner ports were positioned to divide the 16-cell structure approximately evenly, enabling field tuning over all cells. A loop-type rf coupler developed for the prototype was used [26]. The slit shape of the pumping ports was designed to suppress leakage rf fields.

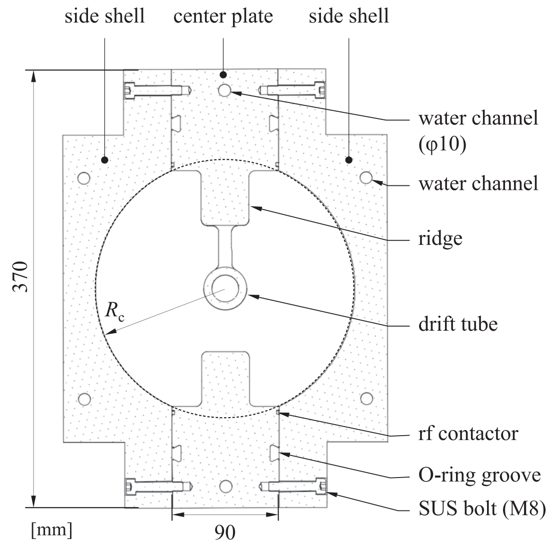

FIG. 5. Cross-sectional front view of the IH-DTL.

Figure 7 is a photograph of the machined center plate of the IH-DTL. Following the machining process, the dimensions of the cavity were assessed using a coordinate measuring machine. The differences between the measured and designed values for all drift tube lengths (L_{DT}) were less than 60 μm. The gap lengths (L_{gap}) between the drift tubes were machined within the tolerance of 100 μm. The assembly of the cavity was completed by stacking and bolting the plate and side shells. This assembly procedure prevented misalignment of the drift tube array. No surface treatment was performed for cost reduction, as in the IH-DTL prototype [20].

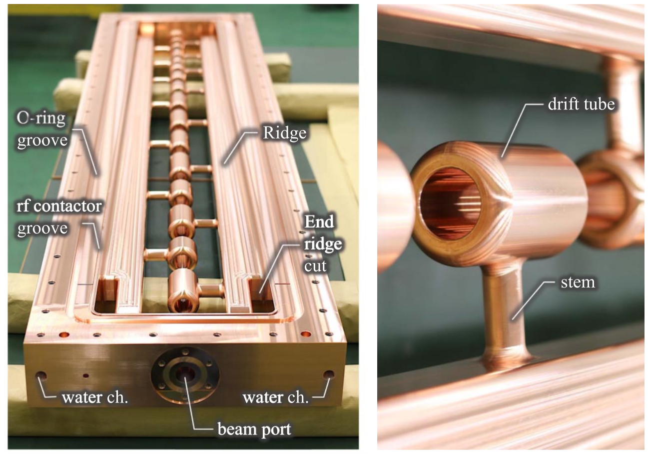

FIG. 7. Fabricated center plate of the IH-DTL.

III. LOW-POWER RF TUNING

First, low-power rf measurements of the resonant frequency and Q_0 were performed for the bare cavity without tuners and the rf coupler. An rf pickup loop antenna made of copper wire was mounted inside the cavity, and the rf response was measured using a vector network analyzer while the cavity was evacuated. Table V summarizes the measured and simulated resonant frequencies and Q_0 values for the operating mode. The measured Q_0 corresponded to 92.4% of the simulated value.

Following the initial low-power rf measurements, the six tuners and the rf coupler were mounted on the IH-DTL. Before adjusting the tuner insertion lengths, the initial electromagnetic field distribution was measured in air using the bead-pull method [27], with all tuner insertion lengths set to $L_{t1\text{–}6} = 0$ mm. An aluminum spherical bead

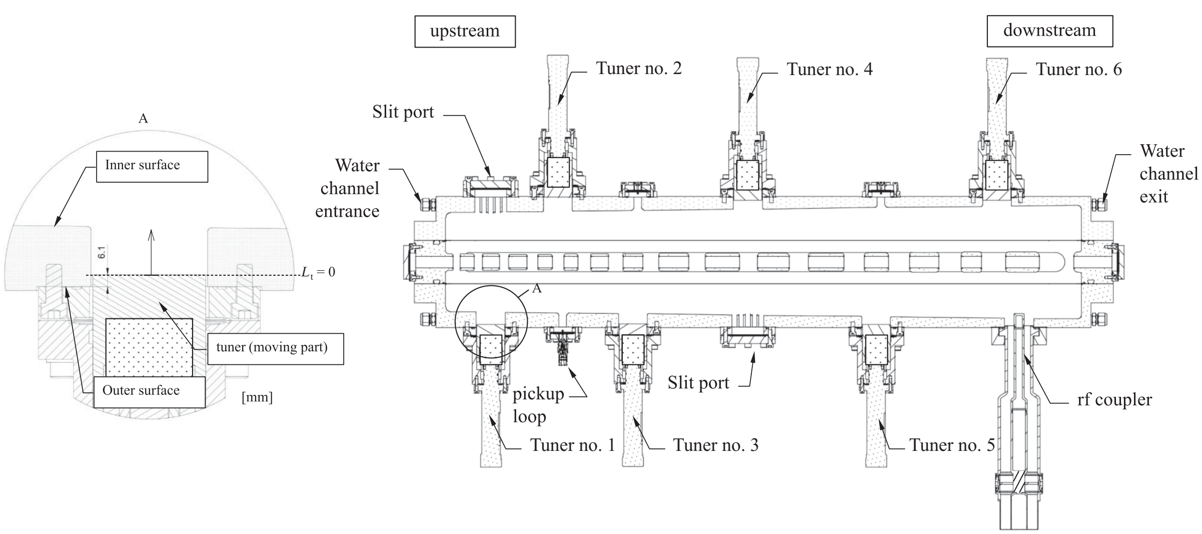

FIG. 6. Top view of the IH-DTL. Under the initial conditions, all tuner insertion lengths were $L_{t1\text{–}6} = 0$ mm, where $L_t = 0$ is defined at the outer surface of the side shell.

TABLE V. Resonant frequency and Q_0 of the bare cavity without tuners and coupler [21].

Parameters	Measurement	Simulation
Quality factor (Q_0)	10080	10910
Resonant frequency (MHz)	322.36	322.38

with a radius of 1.5 mm attached to a thin nylon line was pulled along the beam axis using a stepping motor, and the phase and frequency shifts were measured. Based on the results of the initial bead-pull measurement, the tuner insertion lengths were optimized using a truncated singular value decomposition (TSVD)-based tuning procedure developed with reference to Ref. [28]. The resonant frequency and on-axis field distribution were simultaneously adjusted using this procedure. Details of this procedure are also described in the Appendix.

After low-power tuning, the resonant frequency was measured to be 323.89 MHz at a cavity temperature of 27°C in humid air. This corresponds to the operating frequency of 324.00 MHz under vacuum conditions at the same temperature. Figure 8 shows the measured and simulated frequency shift on the beam axis after low-power tuning. The frequency shift is proportional to $(\varepsilon_0 E^2 - \mu_0 H^2)/2$, where ε_0 is the permittivity of vacuum, E is the magnitude of the electric field, μ_0 is the permeability of vacuum, and H is the magnitude of the magnetic field. Figure 9 shows the relative field error obtained from the difference between the square roots of the measured and simulated frequency shifts. The horizontal error bars represent the gap regions, and the relative field error indicates the average value within those regions. The vertical error bars come from random measurement errors. The error bars for the first and last cells are larger because they have lower field strength than the others. The peak-to-peak field error was less than 1.4%. This value is

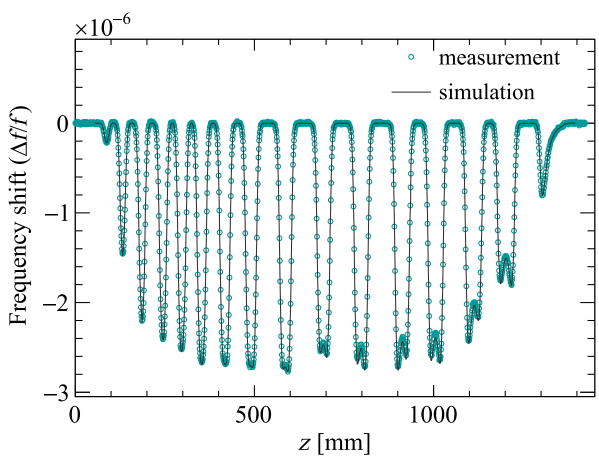

FIG. 8. Measured and simulated frequency shifts obtained by the bead-pull method after low-power tuning.

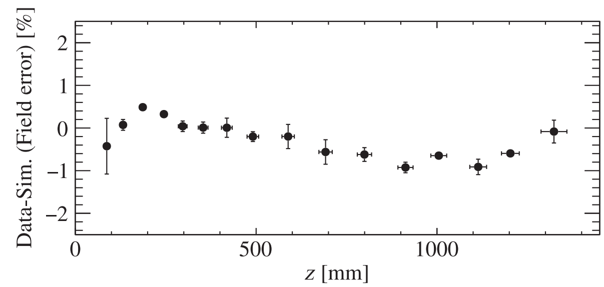

FIG. 9. On-axis field error in the gap regions obtained from the difference between the measured and simulated field distributions.

within the measurement uncertainty associated with the alignment accuracy of the nylon line.

After the bead-pull measurement under atmospheric conditions, the cavity was evacuated, which shifted the resonant frequency close to the operating frequency. A small manual adjustment using tuners no. 3, 4, and 5 was then applied to fine-tune the resonant frequency to 324.00 MHz. The additional insertion lengths of these tuners were only +0.3 mm, so their effect on the on-axis field distribution was negligibly small. The measured Q_0 after the tuning was 8800, corresponding to 83% of the simulated Q_0. The reduction in Q_0 caused by the insertion of tuners without rf contactors was sufficiently small for operation. The coupling coefficient of the rf coupler during high-power operation was set to $\beta_{\mathrm{coupler}} = 0.85$. Critical coupling is preferable because beam loading is negligible for the accelerated muon beam. The rf coupler had originally been constructed for the prototype cavity [20]; for this coupler, the coupling could be adjusted by rotating the rigid loop, whereas the insertion depth was fixed. This setting was the maximum obtainable without modifying the coupler structure; consequently, the cavity was operated undercoupled. The existing coupler was used without modification because the available klystron power was sufficient for the high-power test. Based on the measured Q_0 and coupling coefficient, a peak power of 390 kW is required to achieve the nominal voltage. Table VI summarizes the results of the low-power tuning.

IV. HIGH-POWER TEST

Figure 10 shows the experimental setup of the high-power test. The IH-DTL was installed in the Linac building at J-PARC. The high-power test system consists of the IH-DTL cavity, a 324-MHz klystron (Canon E3740A [29]), waveguides (WR2300), a circulator, coaxial lines (WX203D, WX152D, and WX77D), a directional coupler, the rf coupler, a low-level rf control system, and a water-cooling system. Two slit ports were prepared for cavity evacuation, but in this experiment, only the middle port, located opposite tuner no. 4, was attached to a 240 L/s turbomolecular pump (TMP).

TABLE VI. Tuner insertion lengths after low-power tuning, referenced to the outer surface of the side shell, together with the results of low-power measurements in vacuum.

Tuner no.	Tuner insertion length
1	37.68 mm
2	37.57 mm
3	34.34 mm
4	39.32 mm
5	35.79 mm
6	39.96 mm

Parameters	Values
Measured resonant frequency	324.00 MHz
Measured Q_0	8800
Simulated Q_0	10600
β_{coupler}	0.85
Required rf power	390 kW

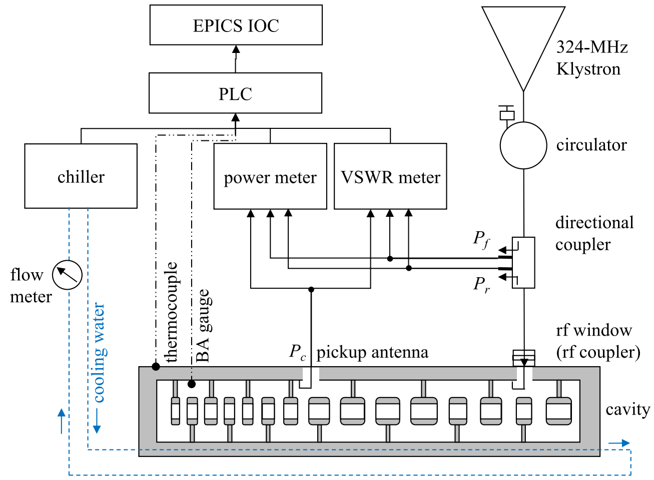

FIG. 11. Block diagram of the rf and cooling system for high-power operation. The interlock is triggered by the rf power and VSWR of the input and reflected waves, vacuum pressure, and cavity temperature.

The pressure in the cavity was constantly monitored with a Bayard-Alpert (BA) gauge attached to the port located opposite tuner no. 5.

Figure 11 shows the block diagram of the rf and cooling system for the high-power test. The rf power and VSWR of the input and reflected waves were measured using a power meter (SPANAWAVE 8542 C [30]) and a VSWR (voltage standing wave ratio) meter [31]. The cavity standing wave was monitored via the pickup loop antenna. The primary cooling water was cooled and maintained to 27 ± 0.1°C by a dc inverter chiller (ORION RKE5500B-V-SP [32]). The cooling water was divided into six branches and supplied to the six cooling channels in the cavity. The flow rates at all channel exits were measured using float-type flow meters, and the flow rates for each channel were adjusted to 4.4 L/ min /ch. The flow rate for each channel was determined from a heat-transfer calculation using the Dittus-Boelter equation [33], assuming a 1°C temperature rise of the cooling water through the cavity during operation. During high-power operation, the cavity temperature was monitored by the three thermocouples mounted on the outer wall of the cavity. These data were recorded by an experimental physics and industrial control system input/output controller (EPICS IOC) via a programmable logic controller (PLC).

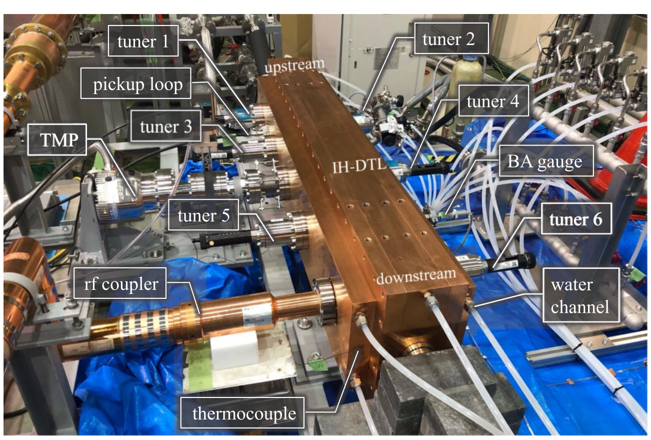

FIG. 10. Photograph of the experimental setup of the high-power test.

An interlock system automatically turns off the rf power when the input or reflected rf power, VSWR, vacuum pressure, or cavity temperature exceeds preset limits. The limit of the reflected rf power (P_r) was set to 70 kW to reduce the risk of damage to the rf coupler window due to discharge. Furthermore, a quick recovery system [34] was used to automatically restore rf operation after trips during high-power conditioning. This system restored rf operation within 1 s after a trip.

Figure 12 shows the conditioning histories of the cavity power (P_c), the pressure in the cavity, and the temperature of the outer wall of the cavity. The high-power test was performed intermittently during daytime operation, and the horizontal axis represents the accumulated rf-on time. The conditioning proceeded first at half the required duty factor of 0.05% with a pulse width of 20 μs and a repetition rate of 25 Hz. After reaching the nominal power of 390 kW, the operation was switched to the required duty of 0.1% with a pulse width of 40 μs and a repetition rate of 25 Hz. After 18 h of conditioning, the nominal power was reached at the nominal duty factor. The frequency of rf trips gradually decreased as conditioning proceeded at the nominal power. The water-cooling system kept the temperature of the cavity stable within 27.0 ± 0.5°C. No additional frequency tuning was required during operation, indicating that the cooling system operated effectively within the acceptable range of cavity power dissipation.

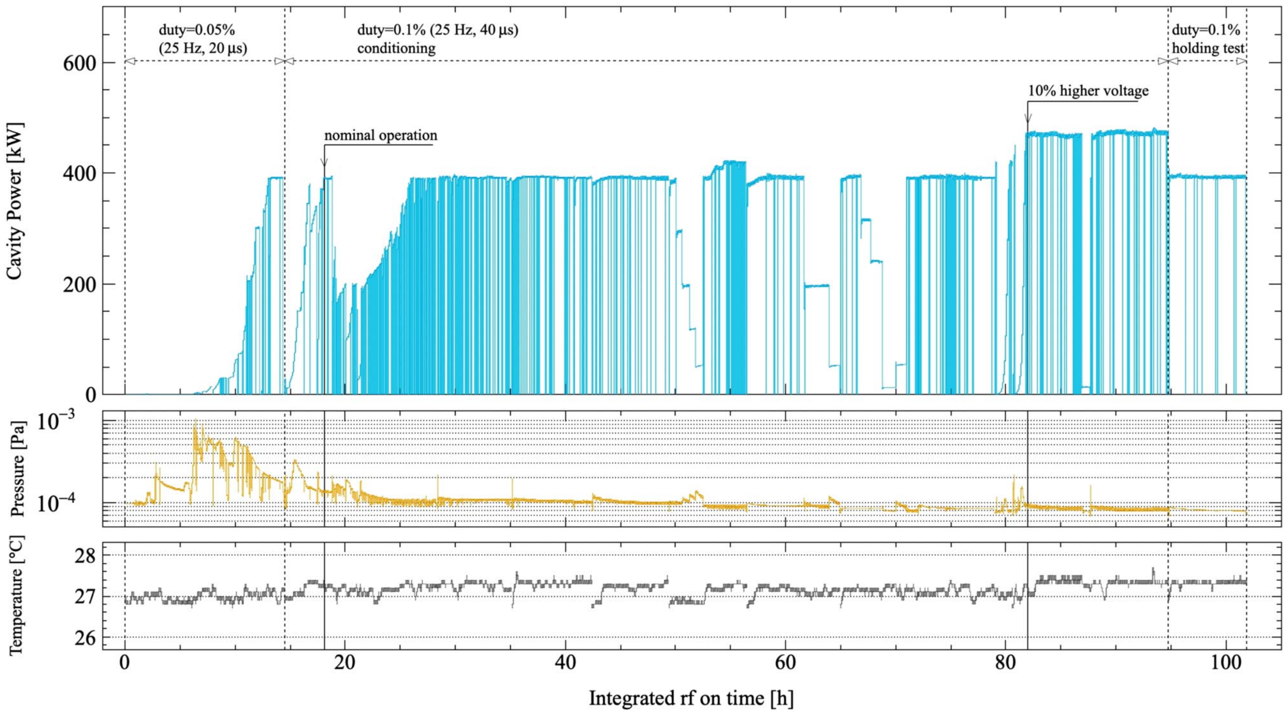

FIG. 12. Conditioning history of the cavity power (top), pressure (middle), and temperature (bottom) of the IH-DTL. This graph shows the data points per second. The temperature data represent the average of three thermocouples mounted at different locations on the outer wall of the cavity. No significant temperature difference was observed among the measurement locations.

After 82 h of conditioning, high-power operation beyond the nominal power was performed to verify stable operation with an additional power margin. The cavity power reached 470 kW, corresponding to an accelerating field of 4.0 MV/m. This value exceeds the design accelerating field of 3.6 MV/m by 10%.

Following a conditioning period of 94 h, a nominal power-holding test was conducted. During a 7-h operation, rf trips occurred 9 times. Thanks to the quick recovery system, the total downtime fraction during this period was 0.04%. These results demonstrate that the 324-MHz IH-DTL achieved stable operation after an appropriate conditioning process.

V. CONCLUSION

The first full-size 324-MHz APF IH-DTL dedicated to muons was successfully constructed and tested. The IH-DTL adopted a cost-effective three-piece cylindrical cavity structure with monolithic drift tubes. After TSVD-based optimization of the six slug tuner insertion lengths, the peak-to-peak on-axis field error was reduced to less than 1.4% while maintaining the operating frequency. High-power operation demonstrated stable cavity performance at the nominal power of 390 kW without surface treatment. The cavity also achieved a peak power corresponding to an accelerating field of 4.0 MV/m, which is 10% higher than the design value of 3.6 MV/m. In addition, the water-cooling system maintained stable cavity operation without additional frequency tuning during high-power operation. These results demonstrate that the IH-DTL satisfies the rf performance requirements for the precise muon $g-2$ measurement and EDM search at J-PARC.

ACKNOWLEDGMENTS

We thank TIME Co., Ltd. for fabricating the 324-MHz APF IH-DTL. We would like to thank Mitsushi Abe for providing us with information on the truncated singular value decomposition. This work was supported by JSPS KAKENHI Grants No. JP15H03666, No. JP18H03707, No. JP16H03987, No. JP20J21440, No. JP20H05625, No. JP21H05088, No. JP22H00141, and No. JP26K21565, and by the JST FOREST Program under Grant No. JPMJFR212O.

DATA AVAILABILITY

There are no publicly available research data or software supporting this manuscript. Requests for further information or data should be sent to the authors.

APPENDIX: LOW-POWER TUNING METHOD AND PROCEDURE

1. Tuning algorithm

The on-axis electric-field distribution was tuned using higher-order mode mixing [27] induced by local resonant-frequency perturbations. Typically, slug tuners are used to introduce such perturbations [35]. The response function of a slug tuner to the electric-field distribution is usually calculated using analytical methods such as equivalent circuit models [36]. However, the asymmetric structure of the IH-DTL makes it difficult to derive the response function using an equivalent circuit model. Another approach is to measure the response of each tuner experimentally, but this is time-consuming. Therefore, for practical tuning, we used response functions obtained from three-dimensional FEM calculations.

The field variation in each cell depends mainly on mixing with the higher-order TE_{112} mode, which is closest to the operating TE_{111} mode. The tuner position determines the field variation in each cell because the mode mixing depends on the position and strength of the local frequency perturbation. Figure 13 shows the calculated on-axis field variations from the reference electric-field distribution in each cell gap when the jth tuner ($j = 1, \ldots, 6$) is inserted from $L_j = 0$ to 40 mm. When there are multiple perturbation points, the field variations have a linear field tilt [27]. Therefore, assuming that the tuners are inserted sequentially, the response function of the jth tuner was obtained with tuners no. 1 to $j-1$ fixed at an insertion length of 40 mm. This reference insertion length was chosen because tuner insertion lengths of approximately 30–40 mm are required to tune the resonant frequency to 324 MHz. The field variation in each cell was sufficiently linear with respect to the tuner insertion length. The response matrix describing the effect of the tuner insertion lengths on the electric-field distribution is given by

$$\Delta E_i = \sum_j \frac{\partial E_i}{\partial L_j} L_j \; (\Delta\vec{E} = \mathbf{M} \cdot \vec{L}), \tag{A1}$$

where E_i is the on-axis electric field of the ith gap ($i = 1, \ldots, 16$). The matrix element $\partial E_i / \partial L_j$ represents the response of the ith gap field to the insertion length of the jth tuner, and the response matrix is denoted by $\mathbf{M}$. The tuner insertion lengths are formally obtained as

$$\vec{L} = \mathbf{M}^{+} \cdot \Delta\vec{E}, \tag{A2}$$

where $\mathbf{M}^{+}$ is the generalized inverse of $\mathbf{M}$. Because $\mathbf{M}$ is a nonsquare matrix with dimensions 16×6, this tuning problem is treated as an inverse problem.

To solve this inverse problem and obtain reasonable tuner insertion lengths, the TSVD method [28,37] was adopted. The response matrix is factorized as

$$\mathbf{M} = \mathbf{U}\mathbf{\Sigma}\mathbf{V}^{\mathbf{T}}, \tag{A3}$$

$$\mathbf{\Sigma} = \mathrm{diag}(\sigma_j), \tag{A4}$$

where $\mathbf{U}$ and $\mathbf{V}$ are orthogonal matrices, and $\mathbf{\Sigma}$ is a diagonal matrix whose diagonal elements are the singular

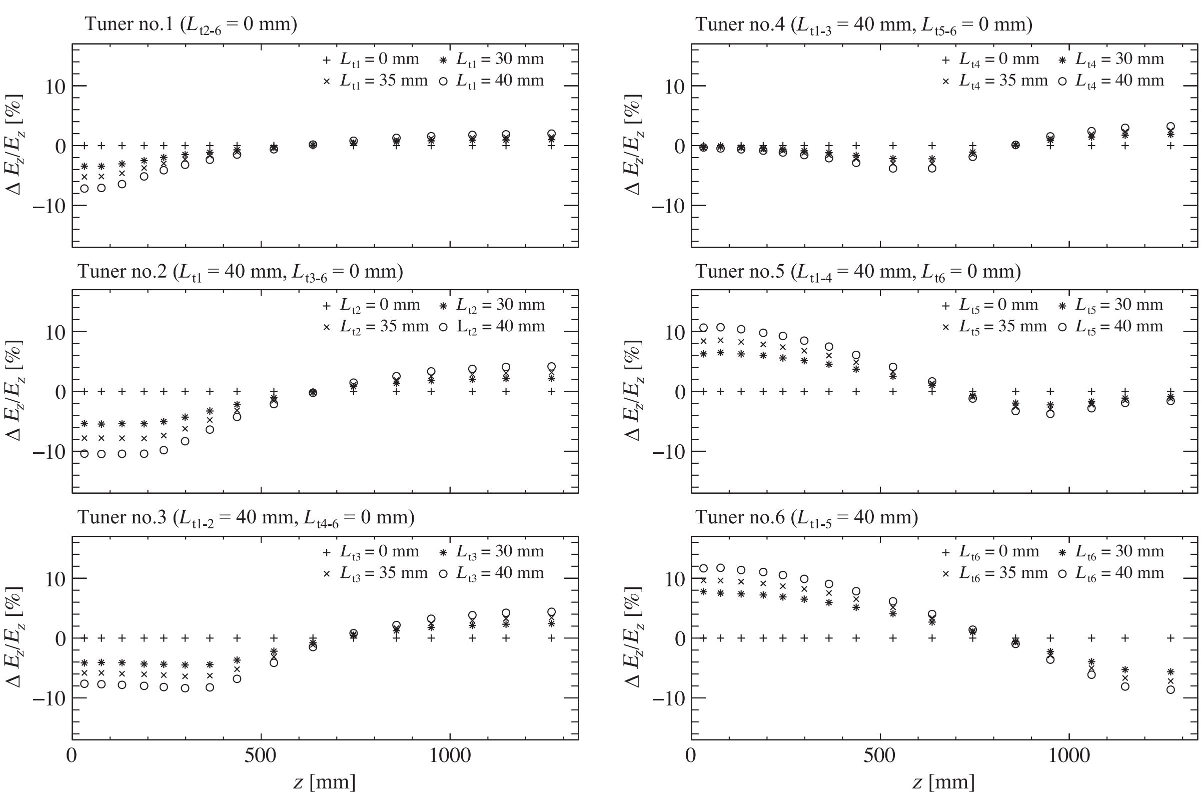

FIG. 13. Simulated on-axis field variation from the reference electric-field distribution in each cell gap.

values σ_j of the response matrix $\mathbf{M}$. The TSVD generalized inverse is given by

$$\mathbf{M}^{+} = \mathbf{V}\mathbf{\Sigma}^{+}\mathbf{U}^{\mathbf{T}}, \tag{A5}$$

$$\mathbf{\Sigma}^{+} = \begin{cases} \frac{1}{\sigma_j} & (j \leqslant t), \\ (t-(j-1))\frac{1}{\sigma_j} & (j-1 \leqslant t < j), \\ 0 & (\text{otherwise}), \end{cases} \tag{A6}$$

where t is a real-valued truncation parameter, referred to as the truncated mode number. For $t = N + \alpha$ with integer N and $0 \leq \alpha < 1$, the singular modes up to the Nth mode are fully included, while only the $(N+1)$th mode is included with a fractional weight α. This method includes only the low-order singular modes required to achieve the target field accuracy, while allowing fine adjustment of the correction strength through noninteger values of t. Furthermore, the frequency response is also linear with respect to the tuner insertion lengths. By constructing a frequency-response matrix, frequency tuning can be performed simultaneously with electric-field correction.

2. Tuning procedure

The low-power tuning procedure using the frequency and electric-field response matrices obtained from FEM calculations is described below.

First, the electromagnetic field distribution was measured using the bead-pull method with all tuner insertion lengths set to $L_j = 0$ mm. In this measurement, the rf coupler was connected to the IH-DTL, and the cavity was filled with air. The measured resonant frequency was 322.22 MHz. Figure 14 shows the field error, defined as the difference between the measured electric-field distribution and the ideal distribution required for muon acceleration. The peak-to-peak field error was about 5.6%. This field error includes fabrication errors and field distortion caused by the additional volume at the tuner ports when the tuners were not inserted to their corresponding flush positions ($L_j \sim 30$ mm), as shown in Fig. 6. Because the field error due to fabrication errors was less than 1.5% in the bead-pull measurement of the bare cavity [38], the dominant contribution to the field error in this measurement was attributed to the latter effect. This distribution was used as the initial field distribution for the tuning algorithm.

The TSVD calculations were iterated using two parameters, the truncated mode number t and the field-amplitude scaling factor, to simultaneously correct the field error and tune the resonant frequency. Figure 15 shows the iterative tuning process, in which the tuner insertion lengths calculated by TSVD were applied and the electric-field distribution and resonant frequency were remeasured. After the first tuning, the peak-to-peak field error was reduced to 2.4%. The residuals between the measured and target field distributions were then used as the input for the next TSVD calculation. After the second tuning, the peak-to-peak field error was reduced to 1.4%, as shown in Fig. 9. The resonant frequency was 323.89 MHz.

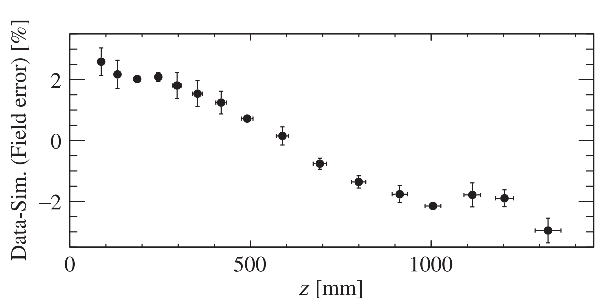

FIG. 14. The field error before low-power tuning. The six tuners and rf coupler were mounted in the IH-DTL. The insertion length of all tuners ($L_{t1\text{–}6}$) was 0 mm. The field error is shown relative to the ideal field distribution for muon acceleration. In this measurement, the resonant frequency was 322.22 MHz.

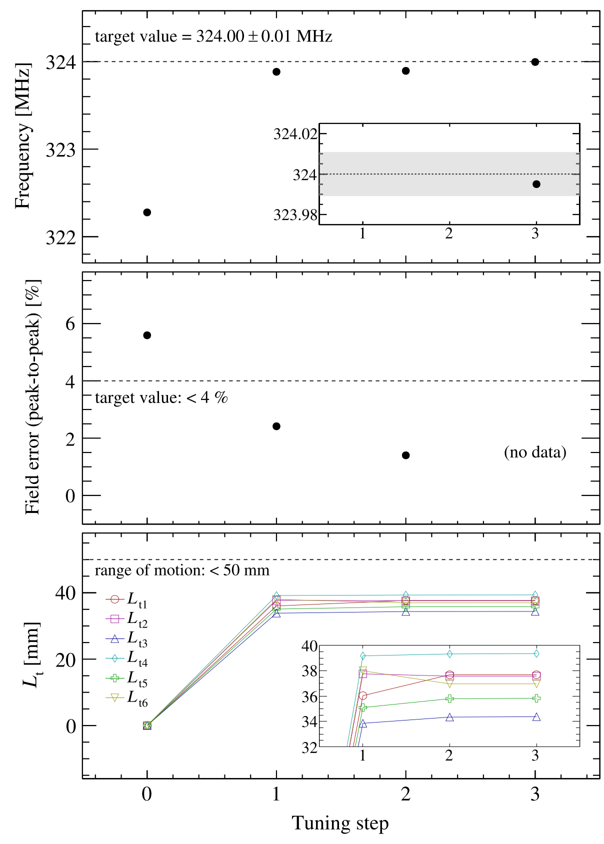

FIG. 15. Frequency and field tuning steps. Step 0: the IH-DTL was under atmospheric conditions with the tuners and rf coupler mounted. All tuner insertion lengths were set to $L_{t1\text{–}6} = 0$ mm. Step 1: the insertion lengths $L_{t1\text{–}6}$ were determined by the first TSVD calculation under atmospheric conditions. Step 2: the insertion lengths $L_{t1\text{–}6}$ were determined by the second TSVD calculation under atmospheric conditions. Step 3: after evacuation of the cavity, a small manual frequency adjustment was performed under vacuum using tuners no. 3, 4, and 5.

The cavity was then evacuated, which shifted the resonant frequency close to the operating frequency of 324.00 MHz. A small manual adjustment was subsequently applied using tuners no. 3, 4, and 5 to fine-tune the frequency. The additional insertion lengths of these tuners were only +0.3 mm. Although no additional bead-pull measurements were performed after this final adjustment, simulations showed that the effect on the electric-field distribution was negligible because of the very small tuner displacement. These results show that the TSVD-based tuning procedure can correct the rf field distribution and resonant frequency within only a few iterations.

[1] D. P. Aguillard *et al.*, Measurement of the positive muon anomalous magnetic moment to 0.20 ppm, Phys. Rev. Lett. **131**, 161802 (2023).

[2] T. Aoyama *et al.*, The anomalous magnetic moment of the muon in the Standard Model, Phys. Rep. **887**, 1 (2020).

[3] R. Aliberti *et al.*, The anomalous magnetic moment of the muon in the Standard Model: An update, Phys. Rep. **1143**, 1 (2025).

[4] M. Abe *et al.*, A new approach for measuring the muon anomalous magnetic moment and electric dipole moment, Prog. Theor. Exp. Phys. **2019**, 053C02 (2019).

[5] M. Otani, First muon acceleration and muon linear accelerator for measuring the muon anomalous magnetic moment and electric dipole moment, Prog. Theor. Exp. Phys. **2022**, 052C01 (2022).

[6] P. Bakule *et al.*, Measurement of muonium emission from silica aerogel, Prog. Theor. Exp. Phys. **2013**, 103C01 (2013).

[7] G. A. Beer *et al.*, Enhancement of muonium emission rate from silica aerogel with a laser-ablated surface, Prog. Theor. Exp. Phys. **2014**, 091C01 (2014).

[8] J. Beare *et al.*, Study of muonium emission from laser-ablated silica aerogel, Prog. Theor. Exp. Phys. **2020**, 123C01 (2020).

[9] Y. Miyake, Y. Nagatani, T. Yamazaki, and P. Strasser, Transmission muon microscope by muon microbeam, realizing 3-d imaging, Microscopy **67**, i3 (2018).

[10] S. Bae *et al.*, First muon acceleration using a radio-frequency accelerator, Phys. Rev. Accel. Beams **21**, 050101 (2018).

[11] Y. Sue *et al.*, Development of a bunch-width monitor for low-intensity muon beam below a few mev, Phys. Rev. Accel. Beams **23**, 022804 (2020).

[12] S. Aritome *et al.*, Acceleration of positive muons by a radio-frequency cavity, Phys. Rev. Lett. **134**, 245001 (2025).

[13] S. S. Kurennoy, Report on study of accelerating structures for muons in the velocity range of beta = v/c = 0.08-0.3 for J-PARC (g-2)/EDM experiment, Tech. Rep. LA-UR-17-20025 (Los Alamos National Laboratory, 2017).

[14] M. Otani, T. Mibe, M. Yoshida, K. Hasegawa, Y. Kondo, N. Hayashizaki, Y. Iwashita, Y. Iwata, R. Kitamura, and N. Saito, Interdigital H-mode drift-tube linac design with alternative phase focusing for muon linac, Phys. Rev. Accel. Beams **19**, 040101 (2016).

[15] S. Minaev and U. Ratzinger, APF or KONUS drift tube structures for medical synchrotron injectors: A comparison, in *Proceedings of the 18th Particle Accelerator Conference* (1999).

[16] Y. Iwata, S. Yamada, T. Murakami, T. Fujimoto, T. Fujisawa, H. Ogawa, N. Miyahara, K. Yamamoto, S. Hojo, Y. Sakamoto, M. Muramatsu, T. Takeuchi, T. Mitsumoto, H. Tsutsui, T. Watanabe, and T. Ueda, Alternating-phase-focused IH-DTL for an injector of heavy-ion medical accelerators, Nucl. Instrum. Methods Phys. Res. Sect. A **569**, 685 (2006).

[17] Y. Iwata, S. Yamada, T. Murakami, T. Fujimoto, T. Fujisawa, H. Ogawa, N. Miyahara, K. Yamamoto, S. Hojo, Y. Sakamoto, M. Muramatsu, T. Takeuchi, T. Mitsumoto, H. Tsutsui, T. Watanabe, and T. Ueda, Performance of a compact injector for heavy-ion medical accelerators, Nucl. Instrum. Methods Phys. Res. Sect. A **572**, 1007 (2007).

[18] P. F. Ma, R. Tang, Y. Yang, S. X. Zheng, W. B. Ye, M. W. Wang, W. L. Liu, B. C. Wang, Q. Z. Xing, C. T. Du, H. Y. Zhang, J. Li, X. L. Guan, X. W. Wang, Z. M. Wang, and M. T. Qiu, Development of a compact 325 MHz proton interdigital H-mode drift tube linac with high shunt impedance, Phys. Rev. Accel. Beams **24**, 020101 (2021).

[19] TIME Co., Ltd., The high-frequency cavity linear accelerators and buncher cavities, Japanese Patent No. 5692905 (P5692905) (Time incorporated company, 2015).

[20] Y. Nakazawa, E. Cicek, K. Futatsukawa, Y. Fuwa, N. Hayashizaki, T. Iijima, H. Iinuma, Y. Iwata, Y. Kondo, T. Mibe, S. Mizobata, T. Morishita, M. Otani, Y. Sue, Y. Takeuchi, and J. Tojo, High-power test of an interdigital H-mode drift tube linac for the J-PARC muon g-2 and electric dipole moment experiment, Phys. Rev. Accel. Beams **25**, 110101 (2022).

[21] Y. Nakazawa, Development of an interdigital H-mode drift tube linac for the J-PARC muon g-2/EDM experiment, Ph. D. thesis, Ibaraki University, 2023, https://rose-ibadai.repo.nii.ac.jp/records/2000011.

[22] Dassault Systèmes, CST MICROWAVE STUDIO / CST studio suite, https://www.cst.com/products/CSTMWS.

[23] W. D. Kilpatrick, Criterion for vacuum sparking designed to include both rf and dc, Rev. Sci. Instrum. **28**, 824 (1957).

[24] Pulsar Physics, General Particle Tracer (GPT), https://www.pulsar.nl/gpt/.

[25] Y. Takeuchi, Development of an RF cavity for muon linac middle-β section for muon g-2/EDM experiment at J-PARC, Ph. D. thesis, Kyushu University, 2023, https://hdl.handle.net/2324/7157288.

[26] Y. Nakazawa *et al.*, Multipacting simulations of coaxial coupler for IH-DTL prototype in muon accelerator, JPS Conf. Proc. **33**, 011128 (2021).

[27] T. Wangler, *RF Linear Accelerators* (Wiley, New York, 2008).

[28] B. Koubek, A. Grudiev, and M. Timmins, RF measurements and tuning of the 750 MHz radio frequency quadrupole, Phys. Rev. Accel. Beams **20**, 080102 (2017).

[29] Canon Electron Tubes & Devices Co., Ltd., Canon E3740A klystron, https://etd.canon/en/index.html.

[30] SPANAWAVE, SPANAWAVE, 8542C dual-input universal power meter, http://www.spanawave.com/store/Model-8542C-Dual-Input-Universal-Power-Meter.asp.

[31] R&K Company Limited, R&K VSWR meter, https://rk-microwave.com/.

[32] ORION Machinery Co., Ltd., ORION RKE5500B-V-SP chiller, https://www.orionkikai.co.jp/english/product/chiller/internal/rke-b/.

[33] W. M. Rohsenow, J. P. Hartnett, and Y. I. Cho, *Handbook of Heat Transfer*, 3rd ed. (McGraw-Hill Education, New York, 1998).

[34] S. Anami, E. Kadokura, S. Michizono, S. Yamaguchi, E. Chishiro, T. Kobayashi, and H. Suzuki, J-PARC linac low level RF control, in *Proc. in the 29th Linear Accelerator Meeting*, 2004).

[35] T. Morishita and Y. Kondo, Electromagnetic design and tuning of the four-vane radio frequency quadrupole with nonuniform intervane voltage profile, Phys. Rev. Accel. Beams **23**, 111003 (2020).

[36] A. Palmieri, F. Grespan, G. Cotto, D. Dattola, and P. Mereu, The IFMIF RFQ Real-scale Aluminum Model: RF Measurements and Tuning, in *Proceedings of the 1st International Particle Accelerator Conference (IPAC'10), Kyoto, Japan* (2010), pp. 603–605, MOPEC061.

[37] G. Golub and C. Van Loan, *Matrix Computations, Johns Hopkins Studies in the Mathematical Sciences* (Johns Hopkins University Press, Baltimore, MD, 2013), https://books.google.co.jp/books?id=X5YfsuCWpxMC&printsec=copyright&hl=en.

[38] Y. Nakazawa *et al.*, Interdigital H-mode drift tube linear accelerator for a muon linear accelerator, Phys. Sci. Forum **8**, 20 (2023).